Chemical Engineering Journal 498 (2024) 155310

Contents lists available at ScienceDirect

Chemical Engineering Journal

journal homepage: www.elsevier.com/locate/cej

Engineering optimal gold nanorod-loaded hollow mesoporous organosilica nanotheranostics for NIR-II photoacoustic microscopy imaging and tumor synergistic therapy

Xin Li [a,b,1], Xuehan Wang [a,b,1], Hongrui Qiu [c], Shiying Li [d], Lik Hang Hugo Tse [a,b], Wai-Sum Lo [a,b], Kwok-Ho Lui [b], Haiyu Zhou [d,*], Yanjuan Gu [a,b,*], Wing-tak Wong [a,b,*]

[a] The Hong Kong Polytechnic University Shenzhen Research Institute, Shenzhen 518057, Guangdong, China
[b] Department of Applied Biology and Chemical Technology, The Hong Kong Polytechnic University, Hung Hom, Hong Kong, China
[c] Guangzhou University of Chinese Medicine, Guangzhou 510006, Guangdong, China
[d] Guangdong Provincial People's Hospital, Guangdong Academy of Medical Sciences, Southern Medical University, Guangzhou 510080, Guangdong, China

ARTICLE INFO

Keywords:
Gold nanorod
Hollow mesoporous organosilica nanoparticles
Photoacoustic microscopy imaging
Second near-infrared (NIR-II) window
Synergistic chemo-photothermal therapy

ABSTRACT

Biodegradable hollow mesoporous organosilica nanoparticles (HMON)-based nanotheranostics has recently gained growing interests due to their tremendous potential as an attractive platform for cancer imaging and therapy. However, the engineering of HMON-based nanotheranostics for size-dependent biological profile on *in vivo* tumor uptake, biodistribution and retention in tumor region have not been achieved to date. Here, a novel tumor microenvironment (TME)-activated nanoplatform employing miniature gold nanorod-loaded HMON (Au@HMON) with tunable hollow cavity of HMON coating is presented, and its application in the second near infrared (NIR-II, 1000–1700 nm) window photoacoustic microscopy (PAM) imaging-guided synergistic chemo-photothermal therapy is studied by loading doxorubicin (DOX). The cancer cell membrane (CCM) biomimetic nanotheranostics (Au@HMON-DOX@CCM) exhibited a high photothermal conversion efficiency of 41.1 % for photothermal therapy (PTT) and PAM imaging. Among the three investigated nanotheranostics, the 221 nm-nanotheranostics exhibited stronger PAM signal and higher drug loading efficacy than the small counterparts (156- and 186-nm) due to the thicker HMON coating layer, larger surface area and intermediate void structure. Therefore, synergistic chemo-photothermal therapy using 221 nm-nanotheranostics is achieved to efficiently inhibit tumor growth. This strategy affords design parameters for engineering HMON-based "all-in-one" nanotheranostics for photoacoustic imaging-guided cancer treatment.

1. Introduction

Recently, the achievement of nanotheranostics depends heavily on the combination of diagnostic approaches and multiple therapeutic modalities into a single nanoplatform. There is an ever-increasing number of papers describing the modification of gold nanorods (AuNRs) for second near-infrared window (NIR-II, 1000–1700 nm) photoacoustic (PA) imaging and photothermal therapy (PTT) owing to its unique plasmonic, acoustic and electric properties, as well as multi-functionality endowed by its various dimensions and morphologies [1–9]. Mesoporous silica (MS)-coated gold nanorods (Au@MS) have attracted a great deal of interest to imaging-guided combined chemo-photothermal therapy [10–12]. The MS shell possesses advantages such as low cytotoxicity, easy functionalization, tunable pore sizes, and high pore volumes that endow mesoporous silica with great loading capacity, which is in favor of encapsulation of various cargo molecules. However, the poor degradability of MS is regarded as an intrinsic drawback seriously impeding their applications in clinical translations. To overcome these drawbacks, some efforts have been made to design mesoporous organosilica nanoparticles (MONs) with controllable biodegradability. A prominent superiority of MON over MS is its diverse framework hybridization of multiple organic moieties, bringing desirable physiochemical performances [13]. The incorporation of functional organic groups such as thioether groups with distinctive disulfide bonds

* Corresponding authors.
E-mail addresses: lungcancer@163.com (H. Zhou), Yanjuan.gu@polyu.edu.hk (Y. Gu), w.t.wong@polyu.edu.hk (W.-t. Wong).
[1] X. Li and X. Wang contributed equally to this work.

https://doi.org/10.1016/j.cej.2024.155310
Received 21 May 2024; Received in revised form 6 August 2024; Accepted 28 August 2024
Available online 11 September 2024

into the framework of HMON gives a specific response to the tumor microenvironment (TME) for stimuli-responsive drug release that enhanced cancer imaging behavior and therapeutic efficacy [14–16]. Moreover, the emerging hollow-structured MONs (HMONs) with an internal cavity provide an enlarged room for drug encapsulation. The fabrication of HMON-based nanotherapeutic platforms through integrating inorganic nanomaterials, including CuS [17,18], Fe_3O_4/Gd_2O_3 [19], AuNRs [20], and organic dye [21] have been widely evaluated for imaging-guided cancer therapy. In spite of the progress, applying HMON-based nanocarrier for *in vivo* imaging and drug delivery is still a major challenge due to the lack of efficiently integrated contrast agents and well-developed surface engineering techniques [22–24]. Therefore, it is imperative to find an optimal strategy to engineer HMON-based "all-in-one" nanotheranostics, not only to improve the stability in physiology environment, but also prevent premature drug leakage and stimuli-release of cargo under the TME-triggers or hyperthermia under imaging-guidance.

PAM is an emerging noninvasive hybrid optical and acoustic imaging technique based on the absorption of light and its conversion to sound [25,26]. Due to the relatively lower scattering and attenuation of the acoustic wave in biological tissue compared to light, the optical resolution of PAM can provide high resolution images at penetration depths of a few millimeters [25]. In addition, the capability of PAM system can be expanded by boosting the sensitivity using exogenous contrast agents such as semiconductor polymers [27,28], NIR dyes [29], and gold nanoparticles (stars, clusters, and rods) [30–32] for tumor diagnosis. However, almost all of these reported gold nanoparticles have an operating window in the first near-infrared (NIR-I) window (650–900 nm). NIR-II PAM imaging offers a higher signal-to-noise ratio, deeper tissue penetration, and better spatio-temporal resolution compared to NIR-I PAM imaging. To date, no study uses NIR-II nanoprobes for improving PAM signal for quantitative assessment of *in vivo* tumor accumulation, biodistribution and clearance studies of different sizes of HMON.

We report, for the first time, a biomimetic NIR-II plasmonic nanotheranostics based on Au@HMON for NIR-II PAM imaging-guided synergistic chemo-photothermal therapy. In this design, three sizes of Au@HMON1-3 were prepared with different sizes of inner cavity of HMON1-3 coating by simply controlling the amount of tetraethylorthosilicate (TEOS) and the pH of the solution (Fig. 1). The nanotheranostics will be used to evaluate *in vivo* the size-dependent effect of HMON-based nanotheranostics on tumor accumulation and

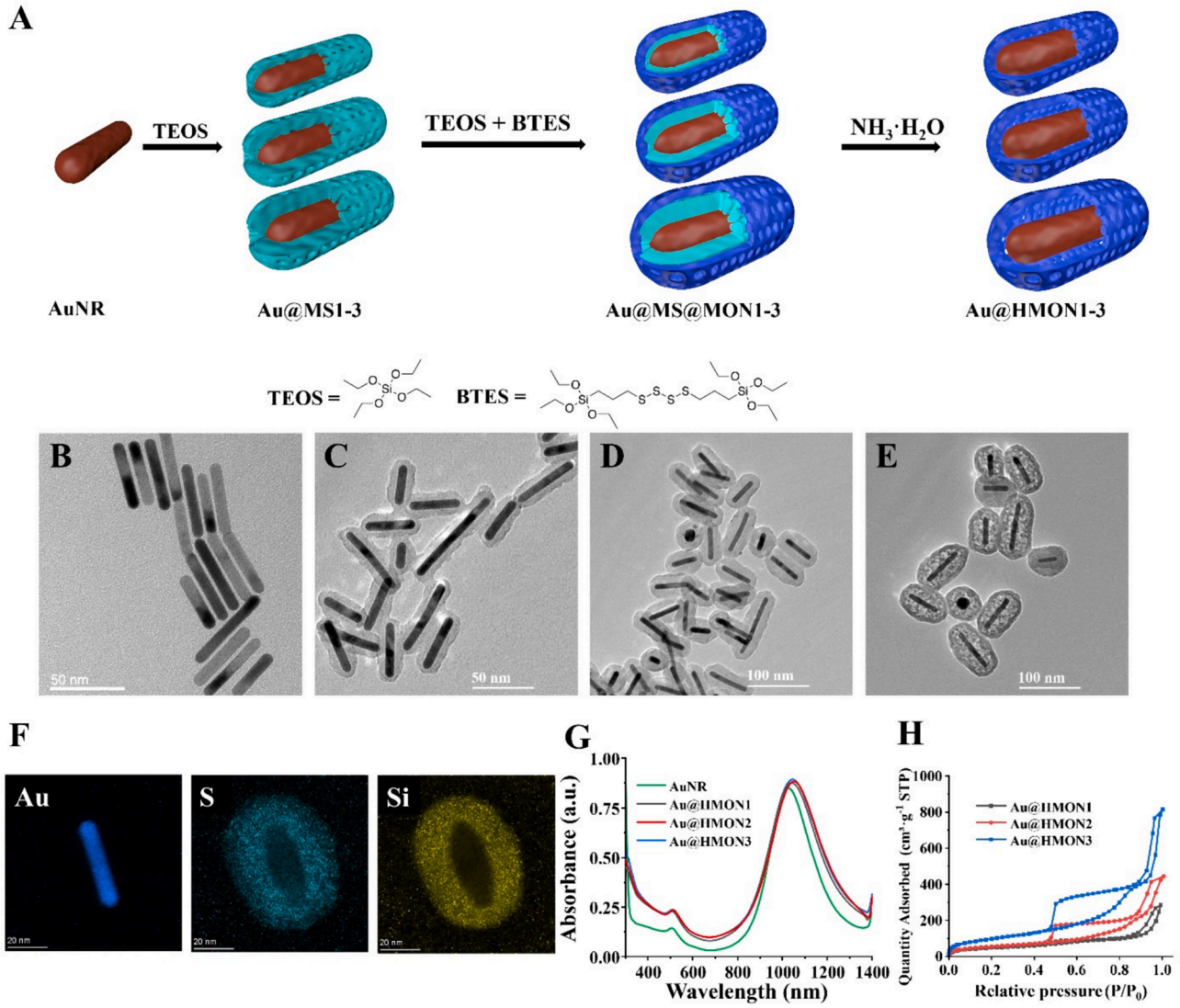

Fig. 1. (A) Scheme for the synthesis of Au@HMON with different cavity size of HMON by simply controlling the amount of TEOS and pH value of solution. TEM images of AuNRs (B), Au@HMON1 (C), Au@HMON2 (D) and Au@HMON3 (E). (F) HAAD-STEM images and element mapping of Au@HMON. Scale bar: 50 nm. (G) Normalized UV–vis-NIR absorption spectra of AuNRs and Au@HMON1-3. (H) N_2 adsorption–desorption isotherms of Au@HMON1-3.

biodistribution using PAM imaging, and to identify the optimal HMON size for the most effective anticancer drug and imaging probe delivery.

After sufficient encapsulation of DOX into the inner cavity and mesoporous pore of Au@HMON, chitosan (CS) was employed as a gatekeeper to covalently link the HMON surface through (3-glycidyloxypropyl)trimethoxysilane (GPTMS), followed by PEGylation with methoxypolyethylene glycol propionic acid (mPEG-COOH) and further modification with 4T1 CCM, which could bestow upon them the intrinsic ability of homologous targeting, increased stability and prolonged blood circulation time. Three sizes (156, 186 and 221 nm) of nanotheranostics were successfully produced and their *in vitro* and *in vivo* NIR-II PAM imaging performance were evaluated. The 221 nm-nanotheranostics were chosen for anticancer effect study owing to its stronger PAM enhancement and larger BET surface areas for higher drug loading efficiency. Under 1064 nm laser irradiation, the pH-, GSH- and hyperthermia-triggered nanotheranostic could improve the DOX release to achieve an enhanced synergistic chemo-photothermal therapy. With the increasing interests in using HMON as a drug delivery cargo, this study provides the potentialities of engineering an optimized HMON-based nanotheranostics for imaging-guided cancer treatment.

2. Experimental

2.1. Materials

Sodium borohydride ($NaBH_4$), cetyltrimethyl ammonium bromide (CTAB), cetyltrimethyl ammonium chloride (CTAC), gold (III) chloride hydrate ($HAuCl_4{\cdot}3H_2O$), silver nitrate ($AgNO_3$), hydroquinone, triethanolamine, 1-ethyl-3-(3-dimethylaminopropyl) carbodiimide (EDC) and acetic acid were purchased from Sigma. Ascorbic acid was purchased from Alfa Aesar. Nitric acid (67 %) was purchased from Avantor. Ammonia water (28 %), hydrochloric acid (37 %) and sodium hydroxide (NaOH) were obtained from Duksan. Diethanolamine, N-hydroxysuccinimide (NHS), tetraethylorthosilicate (TEOS) and bis[3-(triethoxysilyl)propyl] tetrasulfide (BTES) were purchased from Macklin. (3-glycidyloxypropyl)trimethoxysilane (GPTMS) and chitosan (M.W. = 30,000) were purchased from Meryer. PEG_{5000}-COOH was purchased from Bidepharm.

2.2. Characterization

NMR spectra was obtained on Bruker Avance 400 (400 M Hz). The morphology and size of the developed nanostructures was examined by transmission electron microscopy (TEM, JEM-2100F). The N_2 adsorption/desorption isotherms were conducted on on high-performance adsorption analyzer (Micromeritics ASAP 2020 Micropore Analyzer). The hydrodynamic size distribution and zeta potential of nanotheranostics was determined by dynamic light scattering (DLS, Malvern Nano ZS). UV–vis-NIR absorption spectra were measured on an UV-3600 spectrophotometer (Shimadzu, Japan). Thermogravimetric analysis (TGA) was used to determine the mass ratio of chitosan, PEG and CCM on nanotheranostics (TGA/DSC 3 + Thermogravimetric Analyzer). Au concentration was measured by an inductively coupled plasma-mass spectrometry (ICP-MS, AGILENT 7900). The temperature was measured by infrared thermal imaging system Ti450 Infrared Camera (Fluke, USA). The absorbance was recorded at a wavelength of 570 nm using a multi-mode microplate reader CLARIOstar multimode microplate reader (BMG Labtech, Germany). Cellular fluorescence was measured by inverted fluorescence microscope Eclipse Ti2-E Live-cell fluorescence imaging system (Nikon, Japan) and laser confocal microscope TCS SPE machine (Leica, German).

2.3. Synthesis of AuNRs

Miniature AuNRs (width < 10 nm, 20 nm < length < 80 nm) were synthesized by the hydroquinone-based seed-mediated method [33,34]. Briefly, a seed solution was obtained by the addition of freshly prepared 1.8 mL of $NaBH_4$ (10 mM) in 0.010 M of NaOH to 36 mL of $HAuCl_4$ (10 mM) in 0.10 M CTAB under vigorous stirring and keeping the solution unstirred for 2 h before use. A growth solution was prepared by addition of 720 μL of $AgNO_3$ (100 mM) and 240 μL HCl (1.0 M) to 144 mL of $HAuCl_4$ (10 mM) in 0.10 M CTAB solution. Then, 9 mL of 0.10 M hydroquinone was added with gentle mixing to the growth solution to reduce Au (III) to Au (0). After the growth solution turned colorless, the 37.8 ml of seed solution was added and left undisturbed for 18 h before washing twice with Milli-Q water via centrifugation at 15000 rpm. The pellet was resuspended in 40 mL Milli-Q for next step usage.

2.4. Synthesis of Au@MS, Au@MS@MON and Au@HMON

The mesoporous silica-coated AuNR (Au@MS) was performed with minor modified Stöber method [35]. To obtain different thickness of MS coating layer, different amount of 25 % TEOS in methanol and NaOH (0.10 M) were added with 40 mL AuNRs containing 2.5 mM CTAB solution. After addition of TEOS drop by drop, the reaction mixture was kept undisturbed for 24 h at 30 ℃ to obtain Au@MS1-3. Typically, 80 μL of TEOS and 0.4 mL of NaOH were added to prepare Au@MS1. 160 μL TEOS and 0.6 mL of NaOH were applied to prepare Au@MS2. 480 μL TEOS and 1.2 mL of NaOH were added to prepare Au@MS3. The disulfide-hybridized MON-coated Au@MS (Au@MS@MON) was synthesized by a "chemical homology" approach according to reported method with some revision [19]. Typically, 200 mg of CTAC and 120 mg of triethanolamine (TEA) was added into the Au@MS and heated to 90 ℃. Then, a mixture of 200 μL of BTES and 100 μL of TEOS was added into the above dispersion and stirred for 3 h to form Au@MS@MON nanostructure. The product was washed with Milli-Q water and methanol for several times, and then refluxed in 50 mL of methanol containing 500 mg of NH_4NO_3 at 80 ℃ for 24 h to remove excess of CTAC and CTAB. In the following etching process, the obtained Au@MS@MON was centrifuged and re-dispersed into 20 mL of water, followed by the addition of 1.0 mL of ammonia water (28 %). The mixture was heated at 95 ℃ for 6 h to obtain the product of hollow mesoporous organosilica-coated AuNR (Au@HMON).

2.5. Synthesis of Au@HMON@CS, Au@HMON@PEG and Au@HMON@CCM

To obtain chitosan (CS)-functionalized Au@HMON (Au@HMON@CS), 1 % w/v chitosan solution was first prepared by dissolving CS in acetic acid solution (2 %, v/v). 60 μL of acetic acid and 30 μL of GPTMS (99 %) was added into Au@HMON dispersed in ethanol solution and reacted for 3 h at room temperature. After that, 3 mL of CS solution was added to the mixture with sonication and reacted for another 24 h. Finally, the obtained Au@HMON@CS was washed twice with 70 % ethanol by high-speed centrifugation (20000 rpm, 30 mins) and re-dispersed in 3 mL of Milli-Q water. Next, the obtained Au@HMON@CS was added to the mixture which PEG_{5000}-COOH (100 mg), NHS (4.6 mg) and EDC (7.8 mg) dissolved in 2 mL of water, and stirred for 24 h to obtain Au@HMON@PEG. The resulting nanoconjugates was then purified by centrifugation and washed with Milli-Q water. The CCM-modified Au@HMON@PEG (Au@HMON@CCM) nanoconjugates was prepared according to our previous report [36]. To coat CCM onto the nanoconjugates, 0.5 mL of prepared CCM vesicles was mixed with 0.5 mL of PBS containing 2 mg of Au@HMON@CS-PEG with sonication and extruded 20 times through a 400-nm-pore polycarbonate membrane. The product was centrifuged with 8000 rpm at 4 ℃ for 20 mins to remove the uncoating CCM to obtain final formation (Au@HMON@CCM) and re-dispersed in PBS for further experiments.

To facilitate the uptake of nanocarrier, rhodamine (Rh)-NHS was used to label the nanocarrier in the manner of the preparation of targeting Au@HMON@PEG-Rh@CCM and non-targeting Au@HMON@PEG-Rh. Rh-NHS was used to react with Au@HMON@PEG for 3 h,

followed by centrifugation and washing to obtain non-targeting Au@HMON@PEG-Rh. After coating with CCM, the targeting product Au@HMON@PEG-Rh@CCM could be obtained.

2.6. Characterization of Au@HMON1-3 and Au@HMON1-3@CCM by thermogravimetric analysis (TGA)

To determine the mass fraction of the organic component in Au@HMON1-3@CCM, Au@HMON1-3 and Au@HMON1-3@CCM samples were carried out by TGA. Typically, approximately 1 mg of the sample was used to measure the weight loss as the temperature increased from 30 ℃ to 900 ℃ under a nitrogen atmosphere with a flow rate of 60 mL/min.

2.7. Drug encapsulation and in vitro pH, GSH and NIR-responsive drug release

For DOX loading, 10 mL of Au@HMON (200 ppm Au) were mixed with different concentration of DOX solution (0.25, 0.5, 0.75, 1 and 2.5 mg mL^{-1}) for 24 h at room temperature. The DOX-loaded Au@HMON (Au@HMON-DOX) was obtained by centrifugation and then washed with H_2O to remove the redundant DOX. Meanwhile, the CS coating and PEG modification is adopted according to the above-mentioned procedure to produce Au@HMON-DOX@PEG or Au@HMON-DOX@CCM. The loading efficiency of DOX on Au@HMON was measured by the detection of the absorbance of DOX in the initial drug solution and supernatant (490 nm) according to our previous study [37].

To study DOX release rate from nanotheranostics, 1 mL of Au@HMON-DOX@PEG dispersion (DOX: 0.64 mg mL^{-1}) was packaged into the dialysis bags (MWCO: 10 KDa), and immersed in 5 mL PBS with different pH values (pH 7.4 and 6.5) with or without 10 mM of GSH. At specific time points, 0.5 mL of the released solution was collected for determining the DOX concentration using UV–vis-NIR spectrometry. To test the NIR-triggered DOX release, the process was performed under the same condition except that the sample was exposed to an NIR laser (0.75 W cm^{-2}, 5 min) after 1 h incubation.

2.8. Stability and biodegradability measurement of Au@HMON@CCM

The stability of Au@HMON3@CCM dispersed in DI H_2O, PBS, or FBS was evaluated using dynamic light scattering (DLS) at room temperature. The size of Au@HMON3@CCM was recorded at various intervals (0, 1, 2, 3, and 4 days).

The biodegradability of Au@HMON3-DOX@CCM dispersed in pH 6.5 PBS solution containing 10 mM GSH for different incubation times (1, 3, 5 and 7 days). The morphology of nanoparticles was observed by TEM.

2.9. Measurement of photothermal performance of Au@HMON

The NIR-II photothermal effect of Au@HMON1-3 was first evaluated with a fixed concentration of Au (10 ppm), volume (500 μL), and a 1064 nm CW laser (0.75 W cm^{-2}). The temperature changes of different dispersions were monitored every 1 min for 5 mins using an IR thermal imaging camera (Fluke, USA). To investigate the photothermal prosperity of the Au@HMON3, different concentrations (10–50 ppm AuNRs) of Au@HMON3 dispersion (500 μL) were exposed to a 1064 nm laser for 5 min at a power density of 1.0 W cm^{-2}. Moreover, the Au@HMON3 dispersions (20 ppm AuNRs) were exposed to different power densities (0.5, 0.75 and 1.0 W cm^{-2}). To test the photothermal stability of Au@HMON3, 1.0 mL of dispersion (20 ppm AuNRs) was irradiated with 1064 nm laser (0.75 W cm^{-2}) for 10 min and then naturally cooled to room temperature. The turn on/off steps was repeated for 5 cycles. The photothermal conversion efficiency (η) of was then calculated according to our previous publication [36,38].

2.10. In vitro cytotoxicity of nanotheranostics

Murine breast cancer cell 4T1, mouse macrophage cell RAW264.7 and fibroblast cells 3T3 (ATCC) were cultured in Dulbecco's modified Eagle's medium (DMEM) containing 10 % fetal bovine serum (FBS) and 100 units/ml penicillin and 100 μg/ml streptomycin (Thermo Fisher). The cells were incubated in 37℃ in a 5 % CO_2 humidity incubator. For subculturing and harvesting cells, 0.25 % trypsin (Thermo Fisher) was used in all experiments.

The cytotoxicity nanocarrier against 4T1, 3T3 and RAW264.7 cells were measured by using the methyl thiazolyl tetrazolium (MTT) assay. Typically, cells were seeded (5.0 x 10^4) in 96-well microplates at 37 ℃ and incubated overnight. The growth media were replaced with a fresh one containing various concentrations of Au@HMON3@CCM (0, 1, 2.5, 5, 10, 20 and 30 ppm Au). After incubation for 24 h, the media was removed and washed with 1 x PBS. Then 150 μL of MTT solution (0.5 mg mL^{-1} in PBS) was added into each well of the 96-well plate. After additional 4 h of incubation, the growth media were removed and the resulting formazan crystals in each well were dissolved with 150 μL DMSO. The absorbance was recorded at a wavelength of 570 nm using a multi-mode microplate reader.

2.11. In vitro cellular uptake study of Au@HMON3@PEG-Rh@CCM by confocal laser scanning microscopy (CLSM)

4T1 and RAW264.7 cells were seeded in glass-bottom confocal dishes at a density of 5 x 10^4 cells per well and cultured for 24 h. Fresh media containing Au@HMON3@PEG-Rh or Au@HMON3@PEG-Rh@CCM (10 ppm Au) were added to each kind of cell. After incubation for 6 h, the culture medium was removed and cells were washed with PBS, followed by the addition of Hoechst (5 μg mL^{-1}) for 10 mins. After remove Hoechst solution, the fluorescence signal was observed with a CLSM.

2.12. In vitro chemo-photothermal therapy synergistic effect of nanotheranostics

The therapeutic efficacy of nanotherapeutics against 4T1 were measured by using the MTT assay. Typically, 4T1 were seeded (5.0 x 10^4) cells in 96-well microplate at 37 ℃ and cultured for 12 h. After that, 150 μL of fresh medium containing various concentrations of Au@HMON3@CCM and Au@HMON3-DOX@CCM (0, 2.5, 5, and 6.7 μg mL^{-1} DOX, equal to 0, 1.5, 3, and 4 ppm Au) with or without laser was added and incubated for 24 h. Finally, after removed the medium with nanotheranostics and washed with PBS, cell viabilities were determined by MTT assay. For the PTT groups, the cells were preincubated with sample for 6 h and then exposed to a 1064 nm laser for 5 min (0.75 W cm^{-2}), and the corresponding temperature range was maintained at 45–47 ℃ with the help of the infrared thermal imaging system.

2.13. Live/dead cell staining measurement

To directly observe the antitumor efficacy of synergistic therapy, the calcein-AM and PI (Thermo Fisher) costaining assay was performed to further evaluate the cancer cell killing ability *in vitro*. Green emissive calcein AM implies live cells while red emissive PI indicates dead cells. The 4T1 cells were seeded into 48-well plates at a density of 2×10^4 cells per well. Cells are cultured with 300 μL medium containing Au@HMON3@CCM (6 ppm Au) or Au@HMON3-DOX@CCM (6 ppm Au, 10 μg mL^{-1} DOX) each well for 24 h with or without laser irradiation. For the PTT group, the cells were preincubated with sample for 6 h and then exposed to a 1064 nm laser for 5 min (0.75 W cm^{-2}) and further incubation for 18 h. Subsequently, the cells were stained with calcein-AM (5 mL^{-1}) and PI (10 μg mL^{-1}) for 20 min followed by washing with PBS and then observed using fluorescence microscope.

2.14. Animal model and preparation

All animal experiments were performed under the protocol approved by the Animal Center of The Hong Kong Polytechnic University (animal licence no.). To build the xenograft tumor models, female Balb/c mice (5 weeks, 17–20 g) was subcutaneously injected with 100 μL of 3 x 10^6 4T1 cells into the inguinal gland of the mammary fat pad. Studies were initiated until tumors reached 80 mm^3.

2.15. In vitro and in vivo PAM imaging

The *in vitro* sensitivity of Au@HMON1-3@PEG for PAM was evaluated on phantom samples. For PAM imaging, polyurethane tube were used as they have minimal absorption of laser light, resulting in very low induced PA signal amplitude. A group of polyurethane tube (N=4, saline as control) with an inner diameter of 300 μm were filled with AuNRs, Au@HMON1@PEG, Au@HMON2@PEG and Au@HMON3@PEG suspension at a series concentration of 0, 62.5, 125, 250, and 500 ppm.

For *in vivo* PAM imaging, 4T1 tumor-bearing mice were treated with nanotheranostics dispersion (150 μL, 1.7 mg kg^{-1} of Au) via tail vein. PAM images were gained on PA imaging system (PASONO-ANI, Guangdong Photoacoustic Technology) before and after injection at various time points (0, 3, 6, 9, and 24 h) using the custom PAM [39]. The PAM images were acquired using the optical excitation wavelength at 532 nm under laser irradiation of 18mJ cm^{-2} and 1064 nm under laser irradiation of 80mJ cm^{-2}. The resolution of the rastor scanning was 256 x 256 pixels. Optical scanning methods were used to acquire three dimensional volumetric PAM data. Three-dimensional volumeric visualization was rendered using the MATLAB (R2014b, the MathWorks) program. The full-field photoacoustic images (10 x 10 mm^2) were selected for tumor signal change.

2.16. In vivo biodistribution and pharmacokinetic analysis

After the orthotopic tumor volume reached approximately 150 mm^3, the 4T1 tumor-bearing mice were treated with Au@HMON3@CCM (1.7 mg kg^{-1} of Au) via tail vein injection. The mice were then sacrificed at scheduled time intervals (1, 3, 6, 9, 12, 24, 48 and 72 h) post injection. Then the major organs (liver, heart, spleen, and kidney) and tumor were weighted and digested to determine the amount of Au. The biodistributions of the functionalized Au@HMON3@CCM in tissues associated with clearance (liver, spleen, and kidney) as well as the tumor, and heart were measured by inductivley coupled plasma-mass spectrometry (ICP-MS) accroding to previous description [40].

The pharmacokinetics of Au@HMON3@CCM were assessed by collecting blood samples at intervals of 5, 15 min, 0.5, 1, 3, 6, 9, and 24 h. The serum concentrations of Au were determined using ICP-MS. The obtained results were then incorporated into a traditional two-compartment pharmacokinetic model to estimate the half-life.

2.17. Bio-TEM analysis

The tumor tissue was fixed using a solution containing glutaraldehyde (2.5 %) and osmium tetroxide (1 %). Following fixation, the sample underwent dehydration through a graded series of ethanol concentrations (50 %, 70 %, 80 %, and 90 %) and acetone. Subsequently, the specimen was embedded in resin at 4 °C. The ultrathin section was then obtained using an ultramicrotome and placed onto transmission electron microscopy (TEM) grids. Staining with uranyl acetate and lead citrate enhanced contrast, facilitating the examination of tumor organelles and vesicles. Finally, FEI Tecnai G2 TEM was employed to capture high-resolution images.

2.18. In vivo synergistic chemo-photothermal therapy and biosafety

For *in vivo* combined therapy, the 4T1 tumor-bearing BALB/c mice were randomly divided into five groups (n = 5) as followed: saline, Au@HMON3@CCM, Au@HMON3-DOX@CCM, Au@HMON3@CCM +laser, Au@HMON3-DOX@CCM+laser (5 mg kg^{-1} of DOX and 3.1 mg kg^{-1} of Au). The mice were tail vein injected every 2 days for total of 3 injections. For PTT treatment group, the tumor tissues from the two groups of Au@HMON3@CCM+laser and Au@HMON3-DOX@CCM +laser were irradiated by 1064 nm laser at 6 h post-injection (0.75 W cm^{-2}, 5 min). The body weight and tumor size of each group were measured and recorded every 2 days during the treatment. After 21 days of treatment, the mice were sacrificed and their blood, tumor tissues and main organs were harvested and the tumor weights were recorded. Then, all of the tissue samples were fixed for H&E and TUNEL assay. A routine blood analysis of red blood cells (RBCs), white blood cells (WBCs), platelets (PLTs), and hemoglobin (HGB) was performed.

Biochemical analysis of serum was processed to evaluate the functionality of various organs of health mice treated with different groups. The liver function was evaluated by analyzing the levels of albumin (ALB), alanine aminotransferase (ALT), aspartate aminotransferase (AST), and alkaline phosphatase (ALP). The renal function was evaluated using blood urea nitrogen (BUN) and creatinine (CREA), and the gallbladder function was evaluated through the measurement of total bilirubin (TBIL). Other main organs were fixed in 4 % paraformaldehyde, and then H&E stain was used to observe the pathological changes.

2.19. Statistical analysis

All the statistical calculations were performed using Origin 9, GraphPad Prism 8, Flow Jo 10.0 and SPSS22.0 software. The measurement data are shown as mean ± SD. Statistical significance between different groups was determined by the two-tail Student's t tests and one-way ANOVA analysis, and the statistical significance was noted as $^{*}P<0.05$, $^{**}P<0.01$, $^{***}P<0.001$.

3. Results and discussion

3.1. Design, fabrication, and characterization of Au@HMON1-3

Fig. 1A depicts the protocol for preparation of the Au@HMON nanocarriers. First, the miniature AuNRs were synthesized through a seed-mediated growth method using CTAB as stabilizing agent [33,34]. It should be emphasized that the volume of hydrogen chloride (HCl) is the critical parameter to adjust the aspect ratio and NIR-II absorption of AuNRs. Afterward, the obtained CTAB-stabilized AuNRs were coated with a layer of mesoporous silica (MS) via the base-catalyzed hydrolysis of tetraethyl orthosilicate (TEOS), followed by the deposition of a mesoporous organosilica nanoparticles (MON) shell on MS to yield Au@MS@MON through the co-hydrolysis of bis[3-(triethoxysilyl)propyl] tetrasulfide (BTES) and TEOS with the feeding ratio of 2. During the formation of MS coating layer, thickness of MS could be adjusted by controlling the amount of TEOS and pH value of solution, which then contribute to the size of inner cavity in HMON. The CTAC was then eliminated by HCl/ethanol mixture to reduce the potential toxicity. After completely removing CTAC, an ammonia-assisted hot water etching strategy was applied to fabricate hollow structure (Au@HMON) by selectively etching away the MS core of Au@MS@MON while leaving the MON shell intact.

The characterization for Au@HMON and relevant structures are presented in Fig. 1, Figure S2 and Table S1. The AuNRs synthesized by a seed-mediated growth method exhibit a regular rod shape with an aspect ratio of ~ 4.5 (70 x 45 nm) (Fig. 1B). After MS and MON shells formation, a dense coating will be formed around AuNR. Herein, three thickness of MS shells (2.7 ± 0.7, 11.7 ± 0.9 and 20.9 ± 1.9 nm) were coated outside of AuNR (Fig. S2A-C), yielding small-cavity Au@HMON1 (Fig. 1C), intermediate-cavity Au@HMON2 (Fig. 1D) and large-cavity Au@HMON3 (Fig. 1E) accordingly after ammonia etching. The

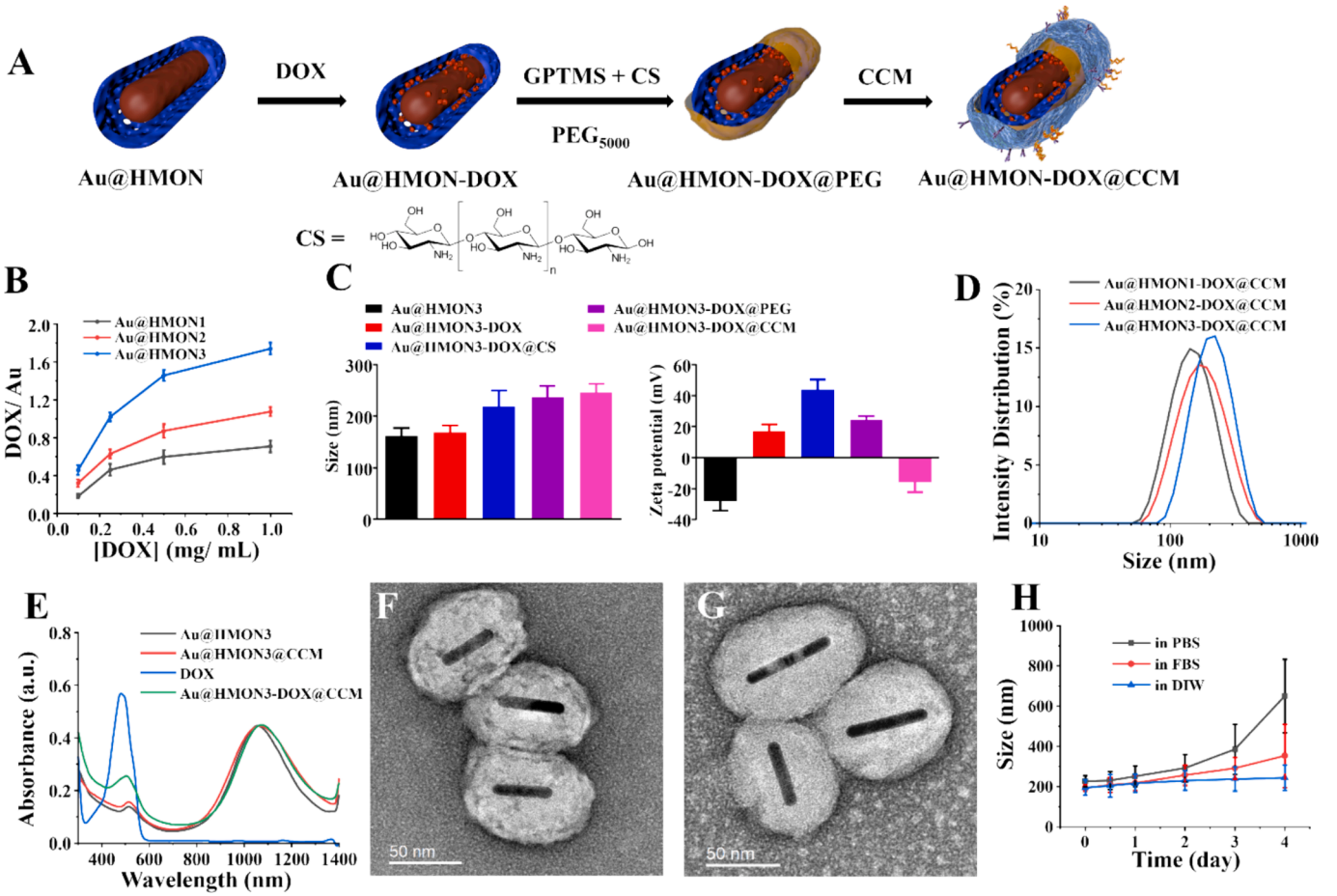

Fig. 2. (A) Scheme for the preparation of Au@HMON-DOX@CCM. (B) Langmuir adsorption isotherms showing the adsorption of DOX by AuNR@HMON1-3. The absorbed DOX was plotted against the initial amount of DOX in the solution. (C) Zeta potential and size distribution of AuNR, Au@HMON3, Au@HMON3-DOX Au@HMON3-DOX@CS, Au@HMON3-DOX@PEG and Au@HMON3-DOX@CCM. (D) Size distribution of Au@HMON1-3-DOX@CCM measured by DLS. The hydrodynamic particle size measured by DLS were 156, 186 and 221 nm for Au@HMON1-DOX@CCM, Au@HMON2-DOX@CCM and Au@HMON3-DOX@CCM respectively. (E) UV–Vis-NIR absorption of nanoconjugates and free DOX. TEM images of (F) Au@HMON3-DOX@PEG and (G) Au@HMON3-DOX@CCM. (H) Evolution of average diameter as determined by DLS for Au@HMON3-DOX@CCM in PBS or serum in 4 days. Data represent mean ± SD, n = 3.

contrast between AuNR and the HMON shell weakened in the TEM image (Fig. 1D and E), indicating that MS cores were completely etched away. However, the contrast between the cavity and HMON shell in Au@HMON1 could not be visually observed due to the small cavity. The as-prepared Au@HMON showed a uniform rattle morphology and each AuNR was well encapsulated inside a uniform and dense HMON shell. Energy-dispersive X-ray (EDX) element maps of Au@HMON3 shown in Fig. 1F further demonstrated that the HMON shell is independently located outside of the AuNR. The size of Au@HMON1-3, statistically measured based on TEM images, is 54.9 ± 9.1, 79.5 ± 11.8 and 89.1 ± 11.5 nm in length and 20.6 ± 1.5, 38.2 ± 2.9 and 57.4 ± 3.5 nm in width, respectively, and the silica shell thickness of all is around 3–4 nm (Table S1). The mass ratios of Au to HMON in the Au@HMON1-3 were 1: 2.25, 1: 3.1 and 1: 4.35, respectively, as determined by inductively coupled plasma mass spectroscopy (ICP-MS). In addition, the FTIR results suggested that CTAC was completely removed from Au@HMON, as revealed by the disappearance of the typical absorption bands of C-H groups (1480 cm^{-1}) (Fig. S3).

The optical properties of AuNR and Au@HMON1-3 were also studied with UV–vis-NIR spectra (Fig. 1G). The formed AuNR displayed two characteristic peaks including the longitudinal surface plasmon resonance (LSPR) peak at 1030 nm and transverse surface plasmon resonance (TSPR) peak at 510 nm. The AuNR spectral shape did not significantly change with the formation of the MON shell, but a slight red shift was observed in the LSPR peak of Au@HMON (1030 nm to 1050 nm) due to the increase in the refractive index from the silica shell around the AuNR [41]. It is worth noting that the intensity of LSPR maintained amongst Au@HMON1-3, indicating that the presence of HMON with 3–4 nm thickness has a negligible effect on the LSPR intensity of AuNRs, which is similar to previous studies on MS-coated AuNR of similar sizes [35]. The BET surface areas of Au@HMON1-3 determined by N_2 adsorption–desorption isotherm assays were 112.8, 199.5, 364.5 m^2/g (Fig. 1H, Table S1), a result of their DOX encapsulation. The average pore size of Au@HMON1-3 were found to be 3.5, 3.5, 3.7 nm (Fig. S4), respectively.

3.2. *Design, fabrication, and characterization of Au@HMON1-3-DOX@CCM*

Surface engineering plays a vital role in *in vivo* application of nanotheranostics. Fig. 2A shows the major steps involved in the synthesis of multifunctional Au@HMON-based nanotheranostics. The complexes of Au@HMON-DOX were readily formed by simply mixing a Au@HMON solution with DOX for 24 h at room temperature followed by washing away unbound DOX. To prevent DOX leakage during circulation in the bloodstream, CS was covalently anchored on HMONs by GPTMS as a crosslinking agent to block the pores of HMON, followed by PEGylation *via* amidation reaction with PEG_{5000}-COOH to render stability in aqueous biological buffers. Afterward, 4T1 CCM was coated onto the surface of Au@HMON-DOX@PEG to obtain the final product of

Au@HMON-DOX@CCM. Furthermore, the extinction coefficient of Au@HMON-DOX@CCM was obtained by plotting a linear fit of its absorbance against its concentration, i.e. (8.76 ± 1.96) x10^8 M^{-1} cm^{-1} (Fig. S5).

The loading capacity of Au@HMON1-3 toward DOX was investigated. Fig. 2B shows Langmuir adsorption isotherms at room temperature for the adsorption of DOX by Au@HMON1-3, suggesting that the loading efficacy of DOX increased with increasing cavity size of HMON. To use Au@HMON3 as an example, successful functionalization by CS, PEG and CCM was confirmed by TEM, TGA, zeta potential and hydrodynamic size measurement (Fig. 2C). Au@HMON3 has a zeta potential of −35.2 mV in water. The zeta potential reversed after DOX loading to + 16.2 mV, while the hydrodynamic diameter slightly increased. After CS was conjugated onto the surface of the HMON, the zeta potential of CS-modified Au@HMON3-DOX (Au@HMON3-DOX@CS) increased to + 36.2 mV due to the presence of NH_2 groups from CS, while the average hydrodynamic diameter also increased from 180 to 210 nm. After PEGylation with PEG_{5000}-COOH, the zeta potential of Au@HMON3@-PEG was + 18.3 mV, while the average hydrodynamic diameter continuous slightly increased. Finally, the zeta potential of Au@HMON3-DOX@CCM reversed again to −19.2 mV due to the coating of CCM, while the average hydrodynamic diameter slightly decreased. As shown in Fig. 2D and Table S2, Au@HMON3-DOX@CCM has a larger DLS size (221 nm) and wider size distribution than Au@HMON1-DOX@CCM (156 nm) and Au@HMON2-DOX@CCM (186 nm). According to the results of TGA, the mass ratio of the coated layer of CS+PEG+CCM on the surface of Au@HMON was determined (Fig. S6 and Table S3). The loading content of DOX in three nanotheranostics could reach up to 10.6 %, 11.4 %, 13.7 % for Au@HMON1-DOX@CCM, Au@HMON2-DOX@CCM and Au@HMON3-DOX@CCM, respectively (Table S2 and S3). This may be explained by the improved inner cavity size and BET surface area of HMONs. The absorption spectra for free DOX, Au@HMON3, Au@HMON3@CCM, and Au@HMON3-DOX@CCM are presented in Fig. 2E, demonstrating the efficient encapsulation of DOX into the nanostructure. Meanwhile, the absorption spectra showed the LSPR peaks for both Au@HMON@CCM and Au@HMON-DOX@CCM were at 1030 nm. Au@HMON3-DOX@PEG and Au@HMON3-DOX@CCM were also characterized by TEM (Fig. 2F and G). It was noted that the contrast between the cavity and shell of HMON decreased significantly and the hollow core could not be obviously observed due to CS and PEG decoration on the HMON surface. After CCM was cladded to the surface, the rough surface of nanoconjugates became smooth and flat. Furthermore, the distribution of DOX within Au@HMON3-DOX was investigated using EDX mapping (Fig. S8) and nitrogen was identified as the characteristic element associated with DOX. The Si distribution region corresponds to the coverage area of Au@HMON3-DOX, while N is uniformly distributed within the Si element distribution area, indicating that DOX is evenly distributed throughout the entire nanoparticle.

The stability of Au@HMON3@CCM was evaluated by recording the hydrodynamic diameter in PBS (pH 7.4) and 100 % fetal bovine serum (FBS) over time (Fig. 2H). It suggested that Au@HMON3-DOX@CCM showed a relatively good stability in H_2O and serum, but gradually aggregated in neutral PBS solution after incubation at 37 °C for 4 days. The *in vitro* biodegradation of Au@HMON3-DOX@CCM after exposure to 10 mM of GSH in pH 6.5 buffer solution was investigated by TEM (Fig. S9). The images reveal that the hollow structure gradually diminished, and the outer HMON layer underwent progressive decomposition with significant disruption (red arrow) observed on the 7th day, which is similar to previous study [42].

3.3. PAM imaging ability

Before performing *in vivo* PAM imaging, the *in vitro* PA performance of three different sizes of nanotheranostics, phantoms filled with AuNRs, Au@HMON1@CCM, Au@HMON2@CCM and Au@HMON3@CCM at various concentrations (i.e. 0, 62.5, 125, 250 and 500 ppm Au) were prepared and imaged with the PAM imaging system using light at 1064 nm (Fig. S10). Quantitative measurement of PA signals demonstrated a linear relationship with the concentration of AuNRs and Au@HMON@CCM in solution. More importantly, 156 nm-Au@HMON1@CCM (PA signal:148 ± 11), 186 nm-Au@HMON2@CCM (PA signal: 160 ± 14) and 221 nm-Au@HMON3@CCM (PA signal: 179 ± 10) showed at least 2-fold increase to that of AuNRs without HMON coating (PA signal: 81 ± 9.6) at the same concentration of 500 ppm Au (Fig. 3A and B). As the PA intensity relies on converting photons to heat efficiently and the heat diffusing rate, there was a negligible change in the absorption of AuNRs after coating organosilica (Fig. 1G), suggesting that the increase of PA signal comes from the increase of thermal transfer from the gold interface to the ambient signal-generating medium because a system with higher heat diffusion rate allows quicker transfer, resulting in a stronger energy peak and PA intensity [9,43]. Coating a silica layer could significantly enhance heat diffusion as the thermal conductance between Si and water is much higher than that between bulk Au and water, resulting in a higher heat diffuse rate and stronger PA intensity.

Previous studies have successfully demonstrated that the size and surface chemistry of nanotheranostics play a pivotal role in determining their biodistribution, tumor accumulation, and clearance from blood or tumor as well as excretion from body, which were found to influence both the delivery and therapeutic efficiency of the nanotheranostics [44,45]. The *in vivo* tumor accumulation and biodistribution of three different sizes of nanotheranostics were first investigated by PAM imaging to optimize the delivery cargo to the TME. In addition, the PAM images were obtained by using two different wavelengths of 532 and 1064 nm, allowing for imaging the microvasculature from tumor region and nanotheranostics with high sensitivity, respectively. The PAM images, 3D volumetric PAM visualization and quantitative data obtained from region-of-interest (ROI) analysis of these PAM images are shown in Fig. 3C to E. It is worthwhile to note that the tumor profile was always clearly distinguished from the background by PAM imaging (532 nm) due to the rich blood vessels in this area. However, the 1064 nm image does not show clear vascular features because of the low pulse energy and weak blood absorption at 1064 nm. No PAM signal at 1064 nm was detected before injection of nanotheranostics in the tumor site due to the low absorption of hemoglobin within blood vessels at that wavelength. After injection, the PA signal from 1064 nm in the tumor region gradually increased and reached a maximum at 6 h post-injection for Au@HMON2-DOX@CCM (186 nm) and Au@HMON3-DOX@CCM (221 nm), while Au@HMON1-DOX@CCM (156 nm) reached the highest signal at 9 h post-injection. In addition, quantitative PA analysis measured from the ROI in the maximum PA images showed that the PA signal enhanced approximately 19.9-, 20.6- and 19.1-fold over that of the pre-injection signal for Au@HMON1-DOX@CCM, Au@HMON2-DOX@CCM, Au@HMON3-DOX@CCM, respectively. With prolonged time, the PA signal in tumor weakened, but there was still a noticeable signal after 24 h. Based on the stronger PAM signal enhancement, higher drug loading efficiency and longer retention time in tumor region of Au@HMON3-DOX@CCM, it was selected as the optimal delivery system in this work for the *in vitro* and *in vivo* synergistic therapy.

3.4. NIR-II photothermal performance of Au@HMON3@PEG

Experimental results found that the temperature of all Au@HMON1-3 dispersions increased by approximately 33 ℃ under 1064 nm laser irradiation, while the temperature of pure water only increased by 9 ℃, indicating that HMON coating didn't affect the photothermal property of AuNRs (Fig. S11). The photothermal effect of Au@HMON3 was dependent on its concentration as well as laser power density (Fig. 4A and 4B). Moreover, the heating of the aqueous dispersion remained consistent after five laser on–off heating cycles, demonstrating the remarkable photothermal stability of the nanocarriers (Fig. 4C). More importantly, the photothermal conversion efficiency of Au@HMON3

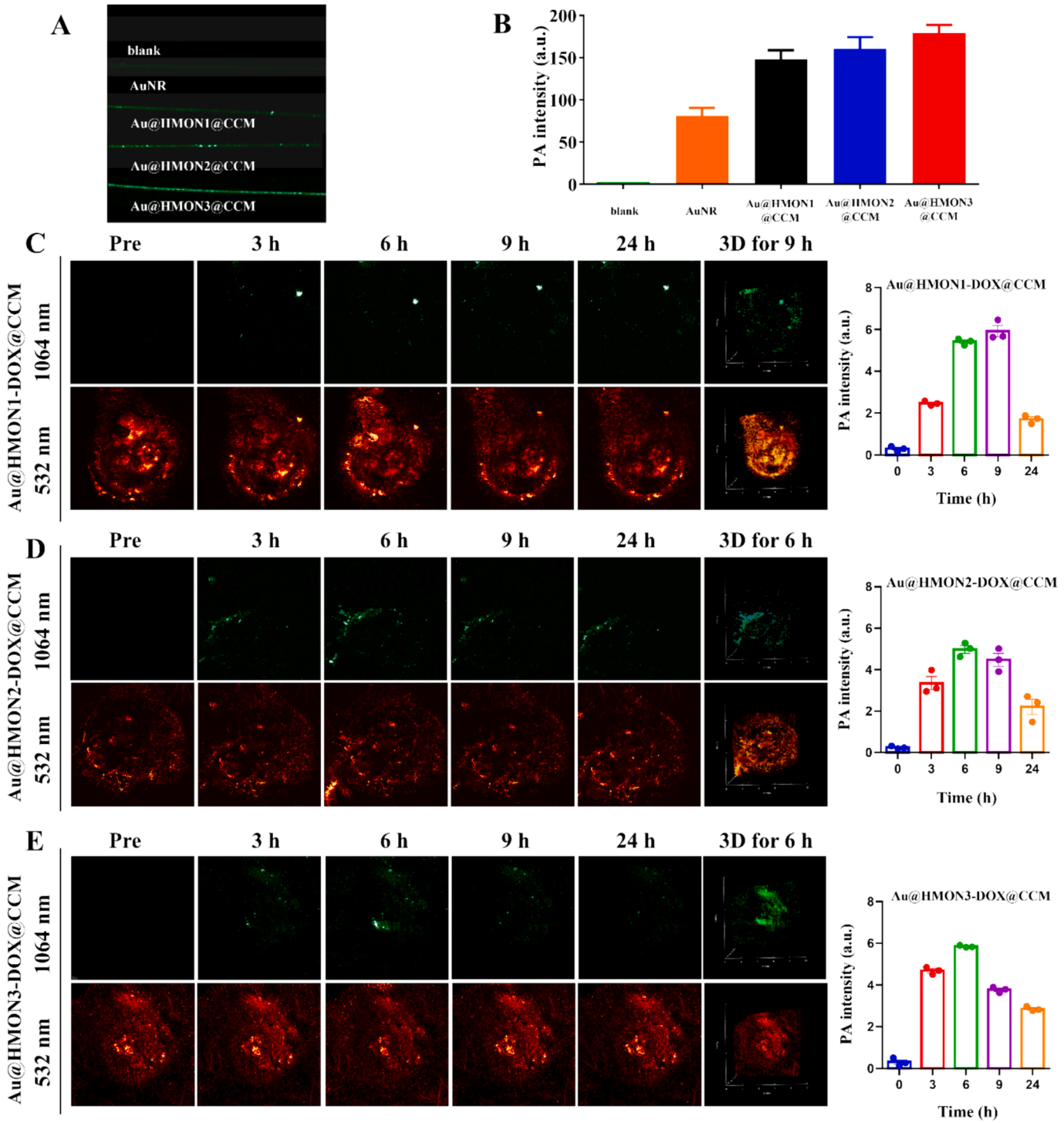

Fig. 3. *In vitro and in vivo* PAM evaluation of nanotheranostics. (A, B) PAM image and its corresponding PA intensity of phantom filled with AuNRs and Au@HMON1-3@CCM at a concentration of 50 ppm acquired at the optical wavelength of 1064 nm under laser irradiation of 80mJ cm^{-2}. (C-E) *In vivo* PAM images and average PA intensities of 4T1 tumors before and at diverse time points after administration of Au@HMON1-DOX@CCM (C), Au@HMON2-DOX@CCM (D) and Au@HMON3-DOX@CCM (E) inside BALB/c mice (Scale bar: 2 mm). *P<0.05, **P<0.01, ***P<0.001.

was calculated to be about 41.1 % at 1064 nm according to our previously reported method (Fig. 4D).

3.5. *In vitro drug release of Au@HMON3-DOX@PEG*

The pH-responsive DOX release profile of Au@HMON3-DOX@PEG was first studied at 37 °C. The cumulative DOX release from Au@HMON3-DOX@PEG was measured in different PBS buffer solutions (pH 7.4 and 6.5) and 10 mM GSH, simulating the physiological environments of blood serum, tumor microenvironments, and intracellular compartments. As shown in Fig. 4E, the amount of released DOX was only 5.0 % after 48 h incubation in pH 7.4 PBS solution, indicating the Au@HMON3-DOX@PEG nanoconjugates have high stability in normal physiological environment, whereas the release amount of DOX reached 23 % within 48 h at pH 6.5 PBS solution. Meanwhile, the GSH-triggered drug release behavior of Au@HMON3-DOX@PEG evident as that the

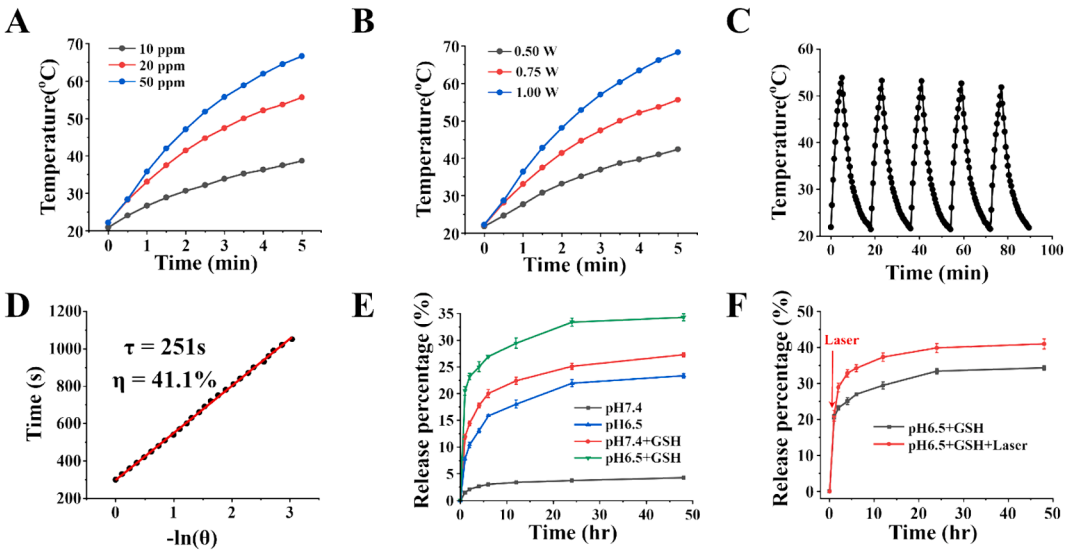

Fig. 4. (A) Temperature change of Au@HMON3 solution at different concentrations under 1064 nm laser (0.75 W cm^{-2}) for 5 min. (B) Temperature change of Au@HMON3 solution (20 ppm Au) at different laser power for 5 min. (C) Temperature records by over five on/off cycles of 1064 nm irradiation at 0.75 W cm^{-2}. (D) The relationship between the linear time data obtained from the cooling time shown in Fig. 4D and −lnΘ. Photothermal conversion efficiency is 41.1 %. (E) *In vitro* DOX release profiles from Au@HMON3-DOX@PEG at different pH values with or without 10 mM GSH. (F) *In vitro* DOX release profiles from Au@HMON3-DOX@PEG in the presence of pH 6.5 + 10 mM GSH with or without 1064 nm laser irradiation (0.75 W cm^{-2}).

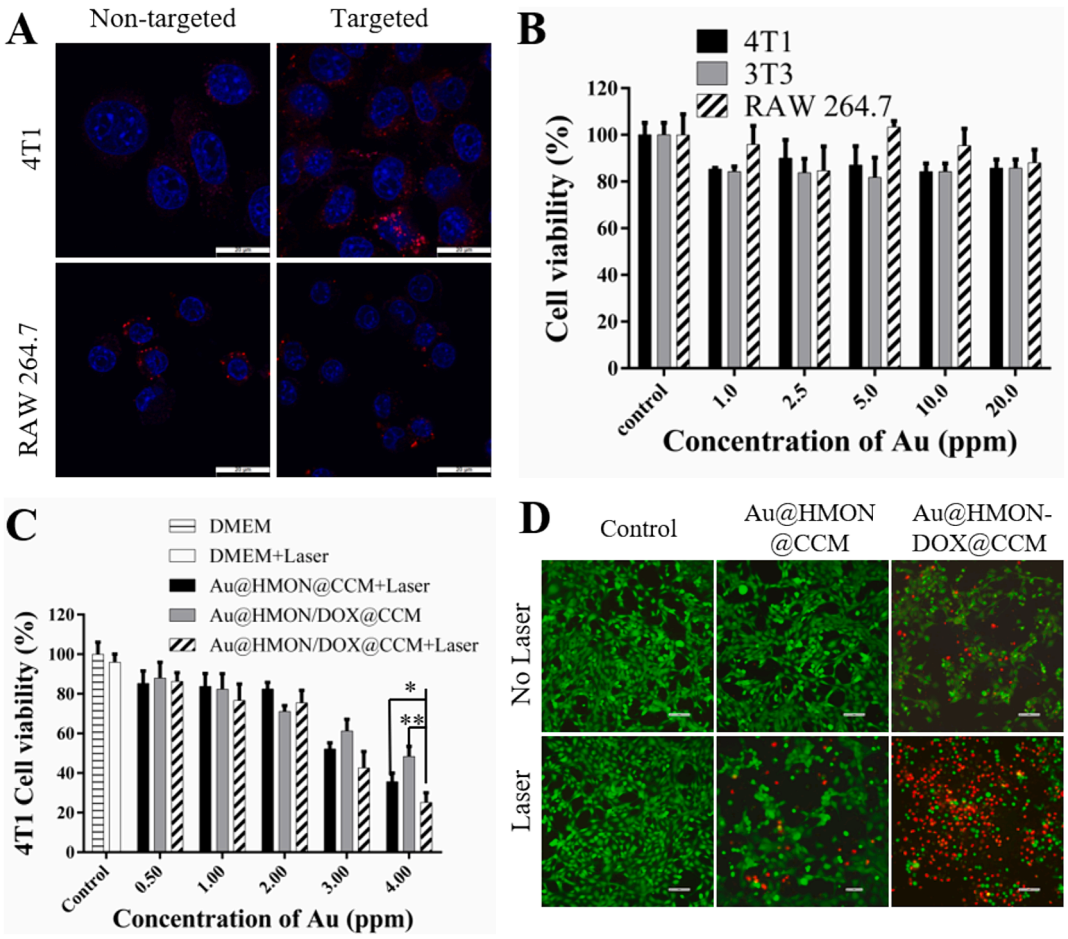

Fig. 5. (A) Confocal images of 4T1 and RAW264.7 cells incubated with Au@HMON3@PEG-Rh@CCM or Au@HMON3@PEG-Rh (10 ppm Au) for 6 h. Scale bar: 20 μm. (B) Relative cell viabilities of 4T1, RAW264.7 and 3T3 cells after incubated with Au@HMON3@CCM for 24 h. (C) MTT of 4T1 cells after various treatments. *P<0.05, **P<0.01. (D) The living cells were stained with green emissive calcein-AM and the dead cells were stained with red emissive PI staining after different treatments with fresh medium, laser only, Au@HMON3@CCM with or without laser, Au@HMON3-DOX@CCM with or without laser (10 μg mL^{-1} DOX, 6 ppm Au, 0.75 W cm^{-2}, 5 min). Scale bars: 100 μm.

cumulative release amount of DOX dramatically increased to 24 % and 30 % after 48 h incubation, respectively, at pH 7.4 and 6.5 in the presence of 10 mM GSH. Furthermore, the accumulated DOX release is increased to 40 % within 48 h at pH 6.5 upon NIR-II laser irradiation (Fig. 4F).

3.6. Cell imaging and viability assay of nanotheranostics

To evaluate the targeting effect of developed nanocarriers, the 4T1 and RAW264.7 cells were treated with Rh-labeled nanocarriers (targeting Au@HMON3@PEG-Rh@CCM and non-targeting Au@HMON3@PEG-Rh) at the same conditions. CLSM was used to observe the localization of nanocarrier *in vitro*. As shown in Fig. 5A, the nanocarrier mainly accumulated in cytoplasm after 6 h incubation. The targeting group exhibited stronger red fluorescence than the non-targeting group in 4T1 cells, suggesting that CCM decoration significantly enhanced tumor cell uptake. In comparison, the targeting group displayed relatively weak fluorescence than the non-targeting group in RAW264.7 cells, verifying that the targeting nanocarrier exhibited excellent homotypic targeting ability and favorable immune evasive efficacy. Furthermore, flow cytometry analysis also demonstrated the enhanced cellular uptake percentages of Au@HMON3@PEG-Rh@CCM (93.8 %) compared to Au@HMON3@PEG-Rh (4.63 %), indicating the remarkable targeting efficiency of CCM (Fig. S12). The cytotoxicity of the nanocarrier was characterized by a standard MTT assay: more than 90 % viability was observed in 4T1, RAW264.7 and 3T3 cells after 24 h treatment even in up to 20 ppm of Au in Au@HMON3@CCM (Fig. 5B), demonstrating the good biocompatibility of nanocarrier.

The *in vitro* synergistic behavior of the nanotheranostics on 4T1 cells was further assessed. 4T1 cells were incubated with Au@HMON3@CCM with or without laser or Au@HMON3-DOX@CCM with or without laser (1064 nm, 0.75 W cm^{-2}, 5 min). As shown in Fig. 5C, NIR-II irradiation alone resulted in a negligible effect on cell viability. In contrast, the viability of 4T1 cells decreased to 50 % after cells were treated with Au@HMON3@CCM+laser (3.0 ppm Au) because of the hyperthermia effect induced by AuNRs, confirming a superior PTT efficacy. For Au@HMON3-DOX@CCM, 40 % of the 4T1 cells were killed due to the loaded DOX and more than 60 % cells were dead after laser treatment was introduced, which could be attributed to the combined effect of photothermal and chemotherapy. Moreover, Au@HMON3-DOX@CCM+laser group showed higher percentage of cell inhibition than that of Au@HMON3-DOX@CCM group or Au@HMON3@CCM+laser group, which could result from the accelerated release of DOX from nanotheranostics by laser-induced hyperthermia of AuNRs. The isobologram analysis reveals that the combination of PTT and chemotherapy from DOX exhibits moderate synergy at a fraction affected (Fa) value of 0.50 (Fig. S13) [46].

To visually evaluate PTT and chemotherapy *in vitro*, green-emissive calcein-AM and red-emissive propidium iodide (PI) were used to stain live and dead cells, respectively (Fig. 5D). Strong green fluorescence was clearly observed in the control, laser alone and Au@HMON3@CCM treatment groups. In contrast, strong red fluorescence was observed in Au@HMON3-DOX@CCM+laser group, while both green and red fluorescence appeared in Au@HMON3-DOX@CCM and Au@HMON3@CCM+laser groups, which was consistent with the MTT results, revealing an enhanced, combined chemo-photothermal effect for *in vitro* cancer therapy.

3.7. In vivo synergistic chemo-PTT effects

The *in vivo* tumor growth inhibition efficacy of Au@HMON3-DOX@CCM was evaluated by 4T1 tumor-bearing BALB/C mice. When the tumor size grew to 100 mm^3, the mice were divided into 5 groups randomly (n = 5), then the mice were intravenously administrated with 150 μL of saline, Au@HMON@CCM, Au@HMON@CCM+laser, Au@HMON-DOX@CCM and Au@HMON-DOX@CCM+laser (DOX of 5 mg kg^{-1} and Au of 3.1 mg kg^{-1}), respectively. After 6 h post-injection, tumor sites of the mice in group Au@HMON@CCM+laser and Au@HMON-DOX@CCM+laser were exposed to 1064 nm laser irradiation for 5 min. The temperature changes of the tumor sites were recorded by infrared thermal imaging and the temperature was found to remain at around 45–47 °C for mild hyperthermia (Fig. 6A and B). *In vivo* antitumor efficacy of various groups was subsequently assessed by monitoring the tumor volume and body weight of mice every two days. As shown in Fig. 6C, concerning the *in vivo* antitumor effects of our nanotheranostics, treatment with Au@HMON@CCM+laser and Au@HMON-DOX@CCM showed minimal effects on suppressing tumor growth when compared to the control group (saline, indicated by a black line). However, Au@HMON-DOX@CCM+laser exhibited a significant effect on suppressing tumor growth, highlighting the anti-tumor efficacy of the synergistic PTT and chemotherapy from encapsulated platform mediated by the cell membrane. The therapy efficacy was also reflected by photographs of the representative tumor tissues after different treatments (Fig. 6D). The body weight of the mice during the treatment period was monitored (Fig. 6E). No obvious body weight loss was observed for all the treatments, suggesting minimal side effects of nanotheranostics under laser irradiation.

To further investigate the synergistic effects and the potential toxicity of Au@HMON-DOX@CCM+laser, histological analysis was performed by haematoxylin and eosin (H&E) staining tumor tissues after different treatments (Fig. 6F). Less purple areas from H&E results were observed in the synergistic group. The terminal deoxynucleotidyl transferase dUTP nick and labeling (TUNEL) assay revealed that Au@HMON-DOX@CCM+laser induced the highest cell apoptosis rate in tumors. Additionally, compared to control, the number of Ki-67 (cell proliferation marker)-expressing positive cells in tumor were significantly reduced upon treatment with Au@HMON-DOX@CCM+laser group. The general toxicity test of nanotheranostics showed that it did not affect the normal range of serum biochemical indicators including alanine aminotransferase (ALT), aspartate transaminase (AST), alkaline phosphatase (ALP), albumin (ALB), total bilirubin (TBIL), creatinine (CREA), blood urea nitrogen (BUN) (Fig. S14). Furthermore, no appreciable histopathological changes were observed in the main organs of the heart, liver, spleen, lung and kidney (Fig. S15), demonstrating its biosafety and low toxicity for cancer imaging and therapy.

3.8. Biodistribution and pharmacokinetic study

To further confirm the tumor uptake of nanotheranostics, the biodistribution of Au@HMON3-DOX@CCM in tumor-bearing mice was investigated by ICP-MS to quantitatively measuring the Au content after intravenous injection of Au@HMON3-DOX@CCM (1.7 mg kg^{-1}). As shown in Fig. 6G, the accumulation of Au at the tumor site exhibited the highest uptake at 6 h post-injection and remained relatively high accumulation at 24 h post-injection, which was in accordance with the PAM imaging results. The biodistribution of Au@HMON3-DOX@PEG was also conducted and compared as a control group shown in Fig. 6H. The Au content in tumor is significantly lower than that in Au@HMON3-DOX@CCM group. It indicated that the enhanced permeation and retention (EPR) effect and CCM mediated endocytosis possibly contributed significantly to the tumor accumulation of nanotheranostics, which is beneficial for imaging and therapy. In addition, abundant Au was detected in the liver and spleen, two major organs in the reticuloendothelial system rich in macrophage that usually act as scavengers to clear nanotheranostics from the bloodstream. The Au content in tumor and organs significantly decreased after 48 and 72 h post i.v. injection of nanotheranostics, indicating efficient clearance of nanotheranostics from the body. The pharmacokinetic and excretion of Au@HMON3-DOX@CCM (Fig. S16) showed that the circulation half-life of Au@HMON3-DOX@CCM (221 nm measured by DLS) *in vivo* was calculated to be 39.7 min, which is more than 3-fold of that of 150 nm PEG-modified HMON (10.8 min) [16], this is likely due to the enhanced

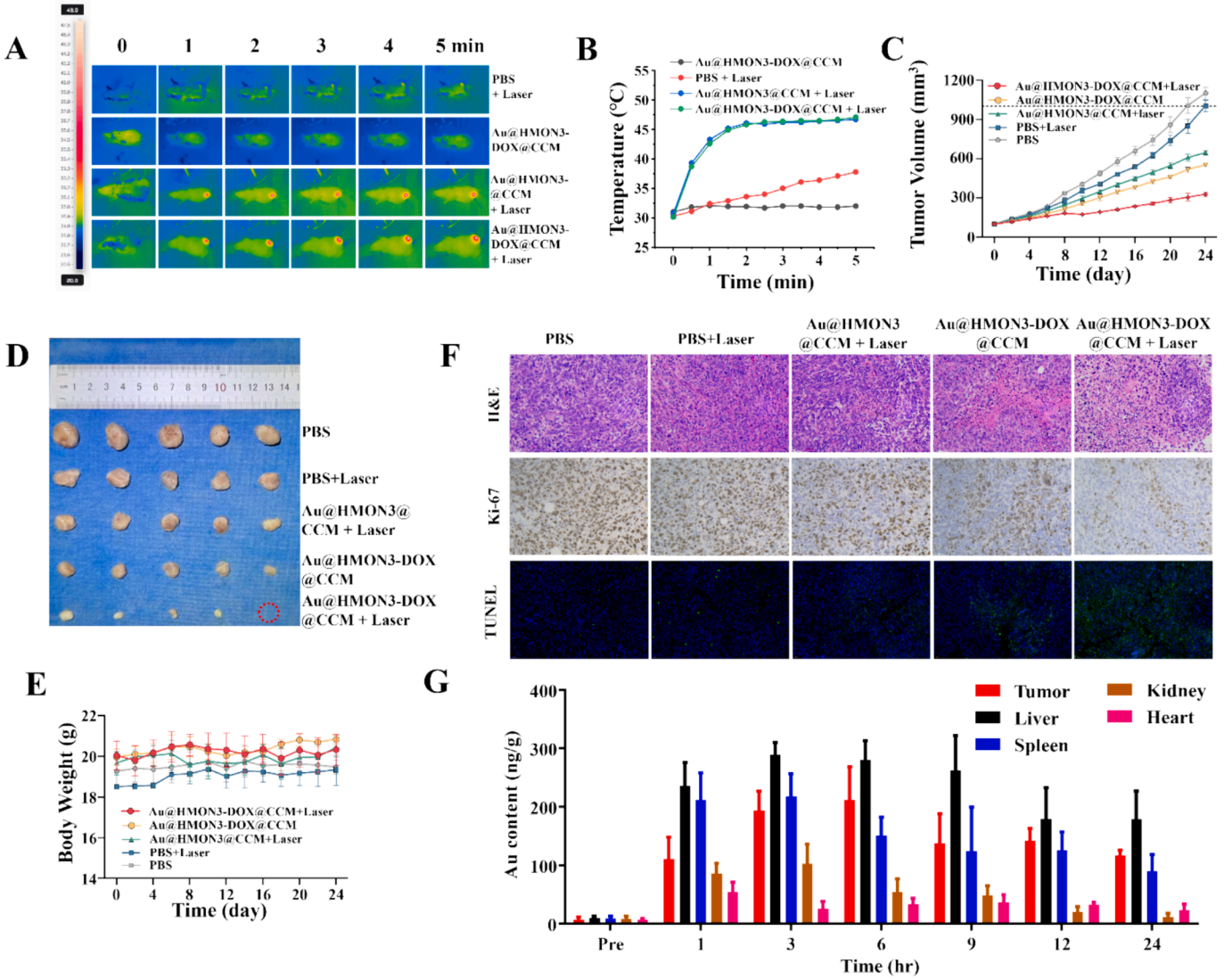

Fig. 6. *In vivo* therapeutic efficacy induced by the Au@HMON3-DOX@CCM nanotheranostics in 4T1 tumor-bearing mice. (A) Thermal imaging and (B) the corresponding temperature plots of tumor sites after i.t. injection of Au@HMON3-DOX@CCM under laser irradiation. (C-E) Therapeutic effect on mice treated with i.t. administration of Au@HMON3-DOX@CCM: *in vivo* 4T1 tumor growth curves in tumor volume (C), photo of tumors (D), and Body weights (E). **P<0.01. (F) Representative histological analysis, including H&E, Ki-67 and TUNEL staining images of tumor sections after different treatments. Scale bars: 100 μm. Data are presented as mean ± SD (n = 5 per group). (G, H) Biodistribution of Au in different organs and tumor of 4T1 tumor-bearing mice at different time point post i.v. injection of Au@HMON3-DOX@CCM (G) and Au@HMON3-DOX@PEG (H). Data are presented as means ± SD (n = 3 per group).

biocompatibility and stability with the triple modification of nanotheranostics. Furthermore, the *in vivo* biodegradation of nanotheranostics was also studied using bio-TEM. As shown in Fig. S17, the morphology of nanoparticles (red arrow) in the tumor region appears mainly as rod-shaped black structures while the elliptical shapes around the rod-shaped structure have disappeared or are barely visible. This suggests the biodegradability of HMON corresponding to the ellipses within the biological system.

4. Conclusions

In summary, we presented novel biomimetic NIR-II AuNRs-encapsulated HMON-based nanocarriers with a tunable hollow cavity of HMON to evaluate the size-dependent biological profiles of organosilica nanoparticles, and identified the 221 nm-nanotheranostics as the most effective delivery vehicle among the three investigated nanotheranostics because of its stronger PA signal enhancement and higher drug loading efficacy. The HMON coating can amplify the PA signal without obviously altering the optical absorption of AuNRs, leading to at least a 2-fold higher PA signal compared with bare AuNRs. Furthermore, the *in vivo* PAM imaging studies showed the maximum tumor accumulation could be achieved at 6 h post-injection and maintained a relatively high tumor accumulation even at 24 h post-injection for 186 and 221-nm nanotheranostics, while the maximum tumor accumulation was reached at 9 h post-injection for 156-nm nanotheranostics. The *in vitro* and *in vivo* effective combinational tumor suppression efficiency was confirmed by the use of Au@HMON3-DOX@CCM. Moreover, the designed nanotheranostics exhibited excellent biocompatibility, biodegradability and negligible systematic toxicities, therefore providing an additional strategy for engineering "all-in-one" nanotheranostics for imaging guided synergistic cancer treatments.

CRediT authorship contribution statement

Xin Li: Writing – original draft, Investigation, Funding acquisition, Data curation. **Xuehan Wang:** Writing – original draft, Investigation, Data curation. **Hongrui Qiu:** Methodology. **Shiying Li:** Methodology, Investigation. **Lik Hang Hugo Tse:** Investigation. **Wai-Sum Lo:** Writing

– review & editing. **Kwok-Ho Lui:** Methodology. **Haiyu Zhou:** Supervision, Resources. **Yanjuan Gu:** Writing – original draft, Supervision, Resources. **Wing-tak Wong:** Supervision, Resources.

Declaration of competing interest

The authors declare that they have no known competing financial interests or personal relationships that could have appeared to influence the work reported in this paper.

Data availability

Data will be made available on request.

Acknowledgements

We acknowledge the grants from the National Natural Science Foundation of China (32071376), and the Research Impact Fund provided by the Research Grants Council of HKSAR, PRC (R5034-18). We also acknowledge the use of facilities in Hong Kong Polytechnic University [University Research Facility for Chemical and Environmental Analysis (UCEA), University Research Facility in Materials Characterization and Device Fabrication (UMF), and University Research Facility in Life Science (ULS)]

Appendix A. Supplementary data

Supplementary data to this article can be found online at https://doi.org/10.1016/j.cej.2024.155310.

References

[1] Y. Lyu, J. Li, K. Pu, Second near-infrared absorbing agents for photoacoustic imaging and photothermal therapy, Small Methods 3 (11) (2019) 1900553.
[2] K. Cai, W. Zhang, M.F. Foda, X. Li, J. Zhang, Y. Zhong, H. Liang, H. Li, H. Han, T. Zhai, Miniature hollow gold nanorods with enhanced effect for in vivo photoacoustic imaging in the NIR-II window, Small 16 (37) (2020) 2002748.
[3] Y. Liu, D. Zhu, J. Luo, X. Chen, L. Gao, W. Liu, T. Chen, NIR-II-activated yolk–shell nanostructures as an intelligent platform for Parkinsonian therapy, ACS Appl. Bio Mater. 3 (10) (2020) 6876–6887.
[4] X. Ge, Q. Fu, L. Su, Z. Li, W. Zhang, T. Chen, H. Yang, J. Song, Light-activated gold nanorod vesicles with NIR-II fluorescence and photoacoustic imaging performances for cancer theranostics, Theranostics 10 (11) (2020) 4809.
[5] J. Ye, Z. Li, Q. Fu, Q. Li, X. Zhang, L. Su, H. Yang, J. Song, Quantitative photoacoustic diagnosis and precise treatment of inflammation in vivo using activatable theranostic nanoprobe, Adv. Funct. Mater. 30 (38) (2020) 2001771.
[6] C. Zhou, L. Zhang, T. Sun, Y. Zhang, Y. Liu, M. Gong, Z. Xu, M. Du, Y. Liu, G. Liu, Activatable NIR-II plasmonic nanotheranostics for efficient photoacoustic imaging and photothermal cancer therapy, Adv. Mater. 33 (3) (2021) 2006532.
[7] T. He, C. Jiang, J. He, Y. Zhang, G. He, J. Wu, J. Lin, X. Zhou, P. Huang, Manganese-dioxide-coating-instructed plasmonic modulation of gold nanorods for activatable duplex-imaging-guided nir-ii photothermal-chemodynamic therapy, Adv. Mater. 33 (13) (2021) 2008540.
[8] Z. Mei, D. Gao, D. Hu, H. Zhou, T. Ma, L. Huang, X. Liu, R. Zheng, H. Zheng, P. Zhao, Activatable NIR-II photoacoustic imaging and photochemical synergistic therapy of MRSA infections using miniature Au/Ag nanorods, Biomaterials 251 (2020) 120092.
[9] W. Yim, J. Zhou, Y. Mantri, M.N. Creyer, C.A. Moore, J.V. Jokerst, Gold nanorod–melanin hybrids for enhanced and prolonged photoacoustic imaging in the near-infrared-II window, ACS Appl. Mater. Interfaces 13 (13) (2021) 14974–14984.
[10] Y. Yu, M. Zhou, W. Zhang, L. Huang, D. Miao, H. Zhu, G. Su, Rattle-type gold nanorods/porous-SiO2 nanocomposites as near-infrared light-activated drug delivery systems for cancer combined chemo–photothermal therapy, Mol. Pharm. 16 (5) (2019) 1929–1938.
[11] J. Wang, J. Liu, Y. Liu, L. Wang, M. Cao, Y. Ji, X. Wu, Y. Xu, B. Bai, Q. Miao, Gd-hybridized plasmonic Au-nanocomposites enhanced tumor-interior drug permeability in multimodal imaging-guided therapy, Adv. Mater. 28 (40) (2016) 8950–8958.
[12] C. Li, K. Feng, N. Xie, W. Zhao, L. Ye, B. Chen, C.-H. Tung, L.-Z. Wu, Mesoporous silica-coated gold nanorods with designable anchor peptides for chemo-photothermal cancer therapy, ACS Appl. Nano Mater. 3 (6) (2020) 5070–5078.
[13] Y. Chen, Q. Meng, M. Wu, S. Wang, P. Xu, H. Chen, Y. Li, L. Zhang, L. Wang, J. Shi, Hollow mesoporous organosilica nanoparticles: a generic intelligent framework-hybridization approach for biomedicine, J. Am. Chem. Soc. 136 (46) (2014) 16326–16334.
[14] J.G. Croissant, Y. Fatieiev, A. Almalik, N.M. Khashab, Mesoporous silica and organosilica nanoparticles: physical chemistry, biosafety, delivery strategies, and biomedical applications, Adv. Healthc. Mater. 7 (4) (2018) 1700831.
[15] Z. Teng, W. Li, Y. Tang, A. Elzatahry, G. Lu, D. Zhao, Mesoporous organosilica hollow nanoparticles: synthesis and applications, Adv. Mater. 31 (38) (2019) 1707612.
[16] W. Fan, N. Lu, Z. Shen, W. Tang, B. Shen, Z. Cui, L. Shan, Z. Yang, Z. Wang, O. Jacobson, Generic synthesis of small-sized hollow mesoporous organosilica nanoparticles for oxygen-independent X-ray-activated synergistic therapy, Nat. Commun. 10 (1) (2019) 1241.
[17] D. Li, T. Zhang, C. Min, H. Huang, D. Tan, W. Gu, Biodegradable theranostic nanoplatforms of albumin-biomineralized nanocomposites modified hollow mesoporous organosilica for photoacoustic imaging guided tumor synergistic therapy, Chem. Eng. J. 388 (2020) 124253.
[18] N. Lu, W. Fan, X. Yi, S. Wang, Z. Wang, R. Tian, O. Jacobson, Y. Liu, B.C. Yung, G. Zhang, Biodegradable hollow mesoporous organosilica nanotheranostics for mild hyperthermia-induced bubble-enhanced oxygen-sensitized radiotherapy, ACS Nano. 12 (2) (2018) 1580–1591.
[19] L. Huang, J. Feng, W. Fan, W. Tang, X. Rong, W. Liao, Z. Wei, Y. Xu, A. Wu, X. Chen, Intelligent pore switch of hollow mesoporous organosilica nanoparticles for high contrast magnetic resonance imaging and tumor-specific chemotherapy, Nano Lett. 21 (22) (2021) 9551–9559.
[20] D. Cheng, Y. Ji, B. Wang, Y. Wang, Y. Tang, Y. Fu, Y. Xu, X. Qian, W. Zhu, Dual-responsive nanohybrid based on degradable silica-coated gold nanorods for triple-combination therapy for breast cancer, Acta Biomater. 128 (2021) 435–446.
[21] Y. Ma, Z. Su, L. Zhou, L. He, Z. Hou, J. Zou, Y. Cai, D. Chang, J. Xie, C. Zhu, Biodegradable metal–organic-framework-gated organosilica for tumor-microenvironment-unlocked glutathione-depletion-enhanced synergistic therapy, Adv. Mater. 34 (12) (2022) 2107560.
[22] T. Yan, J. He, R. Liu, Z. Liu, J. Cheng, Chitosan capped pH-responsive hollow mesoporous silica nanoparticles for targeted chemo-photo combination therapy, Carbohydr. Polym. 231 (2020) 115706.
[23] Z.-T. Lin, C.-H. Gong, L. Tang, B.-L. Cao, F.-S. Kong, Z. Wang, Y.-G. Bi, Study on preparation and in vitro anti-tumor activity of chitosan-modified mesoporous silica hybrids by GPTMS cross-linking agent, React. Funct. Polym. 169 (2021) 105072.
[24] M. Kong, J. Tang, Q. Qiao, T. Wu, Y. Qi, S. Tan, X. Gao, Z. Zhang, Biodegradable hollow mesoporous silica nanoparticles for regulating tumor microenvironment and enhancing antitumor efficiency, Theranostics 7 (13) (2017) 3276.
[25] L.V. Wang, Multiscale photoacoustic microscopy and computed tomography, Nat. Photonics 3 (9) (2009) 503–509.
[26] J. Kim, J.Y. Kim, S. Jeon, J.W. Baik, S.H. Cho, C. Kim, Super-resolution localization photoacoustic microscopy using intrinsic red blood cells as contrast absorbers, Light Sci. Appl. 8 (1) (2019) 103.
[27] J. Chen, Y. Zhang, X. Li, J. Zhu, D. Li, S. Li, C.-S. Lee, L. Wang, Confocal visible/NIR photoacoustic microscopy of tumors with structural, functional, and nanoprobe contrasts, Photonics Res. 8 (12) (2020) 1875–1880.
[28] B. Guo, J. Chen, N. Chen, E. Middha, S. Xu, Y. Pan, M. Wu, K. Li, C. Liu, B. Liu, High-resolution 3D NIR-II photoacoustic imaging of cerebral and tumor vasculatures using conjugated polymer nanoparticles as contrast agent, Adv. Mater. 31 (25) (2019) 1808355.
[29] A.P. Jathoul, J. Laufer, O. Ogunlade, B. Treeby, B. Cox, E. Zhang, P. Johnson, A. R. Pizzey, B. Philip, T. Marafioti, Deep in vivo photoacoustic imaging of mammalian tissues using a tyrosinase-based genetic reporter, Nat. Photonics 9 (4) (2015) 239–246.
[30] V.P. Nguyen, W. Qian, Y. Li, B. Liu, M. Aaberg, J. Henry, W. Zhang, X. Wang, Y. M. Paulus, Chain-like gold nanoparticle clusters for multimodal photoacoustic microscopy and optical coherence tomography enhanced molecular imaging, Nat. Commun. 12 (1) (2021) 34.
[31] V.-P. Nguyen, Y. Li, J. Henry, W. Zhang, M. Aaberg, S. Jones, T. Qian, X. Wang, Y. M. Paulus, Plasmonic gold nanostar-enhanced multimodal photoacoustic microscopy and optical coherence tomography molecular imaging to evaluate choroidal neovascularization, ACS Sens. 5 (10) (2020) 3070–3081.
[32] V.-P. Nguyen, Y. Li, J. Henry, W. Zhang, X. Wang, Y.M. Paulus, Gold nanorod enhanced photoacoustic microscopy and optical coherence tomography of choroidal neovascularization, ACS Appl. Mater. Interfaces 13 (34) (2021) 40214–40228.
[33] Y.-S. Chen, Y. Zhao, S.J. Yoon, S.S. Gambhir, S. Emelianov, Miniature gold nanorods for photoacoustic molecular imaging in the second near-infrared optical window, Nat. Nanotechnol. 14 (5) (2019) 465–472.
[34] H.-H. Chang, C.J. Murphy, Mini gold nanorods with tunable plasmonic peaks beyond 1000 nm, Chem. Mater. 30 (4) (2018) 1427–1435.
[35] Z. Zhao, Q. Guo, L. Cao, S. Jiang, F. Mao, Y. Guo, L. Meng, Z. Wu, Thickness control of mesoporous silica coated on gold nanorod, J. Nanopart. Res. 23 (2021) 1–12.
[36] X. Fang, X. Wu, Z. Li, L. Jiang, W.S. Lo, G. Chen, Y. Gu, W.T. Wong, Biomimetic anti-PD-1 peptide-loaded 2D FePSe3 nanosheets for efficient photothermal and enhanced immune therapy with multimodal MR/PA/thermal imaging, Adv. Sci. 8 (2) (2021) 2003041.
[37] X. Fang, K.-H. Lui, S. Li, W.-S. Lo, X. Li, Y. Gu, W.-T. Wong, Multifunctional nanotheranostic gold nanocage/selenium core-shell for PAI-guided chemo-photothermal synergistic therapy in vivo, Int. J. Nanomedicine 10271–10284 (2020).
[38] S. Li, K.-H. Lui, W.-S. Lau, J. Chen, W.-S. Lo, X. Li, Y.-J. Gu, L.-T. Lin, W.-T. Wong, MSOT-guided nanotheranostics for synergistic mild photothermal therapy and chemotherapy to boost necroptosis/apoptosis, ACS Appl. Mater. Interfaces 14 (29) (2022) 33712–33725.

[39] W. Zhang, X. Luo, F. Yang, Z. Tong, J. Liang, B. Yuan, S. Yang, Z. Wang, Photoacoustic (532 and 1064 nm) and ultrasonic coscanning microscopy for in vivo imaging on small animals: A productized strategy, J Biophotonics 16 (6) (2023) e202300007.
[40] S.K. Balasubramanian, J. Jittiwat, J. Manikandan, C.-N. Ong, E.Y. Liya, W.-Y. Ong, Biodistribution of gold nanoparticles and gene expression changes in the liver and spleen after intravenous administration in rats, Biomaterials 31 (8) (2010) 2034–2042.
[41] J. Wang, W. Zhang, S. Li, D. Miao, G. Qian, G. Su, Engineering of porous silica coated gold nanorods by surface-protected etching and their applications in drug loading and combined cancer therapy, Langmuir 35 (44) (2019) 14238–14247.
[42] P. Li, B. Lin, Z. Chen, P. Liu, J. Liu, W. Li, P. Liu, Z. Guo, C. Chen, Biodegradable hollow mesoporous organosilica nanotheranostics (HMONs) as a versatile platform for multimodal imaging and phototherapeutic-triggered endolysosomal disruption in ovarian cancer, Drug Deliv. 29 (1) (2022) 161–173.
[43] Y.-S. Chen, W. Frey, S. Kim, P. Kruizinga, K. Homan, S. Emelianov, Silica-coated gold nanorods as photoacoustic signal nanoamplifiers, Nano Lett. 11 (2) (2011) 348–354.
[44] S.D. Perrault, C. Walkey, T. Jennings, H.C. Fischer, W.C. Chan, Mediating tumor targeting efficiency of nanoparticles through design, Nano Lett. 9 (5) (2009) 1909–1915.
[45] L. Tang, X. Yang, Q. Yin, K. Cai, H. Wang, I. Chaudhury, C. Yao, Q. Zhou, M. Kwon, J.A. Hartman, Investigating the optimal size of anticancer nanomedicine, Proc. Natl. Acad. Sci. u.s.a. 111 (43) (2014) 15344–15349.
[46] N. Zhang, J.-N. Fu, T.-C. Chou, Synergistic combination of microtubule targeting anticancer fludelone with cytoprotective panaxytriol derived from panax ginseng against MX-1 cells in vitro: experimental design and data analysis using the combination index method, Am. J. Cancer Res. 6 (1) (2016) 97.